PAPER

Check for updates

Mechanical, optical, and thermoelectric properties of α-BaSnS₃ and β-BaSnS₃†

Sihang Wang [ID] and Liping Zhang [ID] *

This study explores the mechanical, optical, and thermoelectric properties of α-BaSnS₃ and β-BaSnS₃ through first-principles calculations. The mechanical analysis reveals that both structures exhibit ductile behaviour. Furthermore, phonon dispersion calculations at 0 K show no imaginary frequencies, confirming their dynamical stability. The electronic structure analysis identifies both compounds as indirect bandgap semiconductors, with a bandgap of 1.63 eV for α-BaSnS₃ and 1.12 eV for β-BaSnS₃. Optical property analysis indicates that both compounds exhibit high absorption coefficients, reaching up to $\sim 10^6$ cm^{-1} in the ultraviolet region and approximately $\sim 10^5$ cm^{-1} in the visible spectrum, demonstrating their potential for optoelectronic applications. To explore the thermal transport properties, we calculated the lattice thermal conductivity using particle-like and wave-like transport channels. At 300 K, α-BaSnS₃ exhibits an average k_p of 1.030 W m^{-1} K^{-1} and k_c of 0.112 W m^{-1} K^{-1}, whereas β-BaSnS₃ exhibits average values of 0.128 W m^{-1} K^{-1} for k_p and 0.179 W m^{-1} K^{-1} for k_c. This reduction in β-BaSnS₃ is primarily attributed to its pronounced anharmonicity and extremely short phonon lifetimes, which predominantly range from 0.1 to 1 ps. In terms of thermoelectric performance, α-BaSnS₃ achieves a *ZT* value of 1.05 at 600 K, while β-BaSnS₃ achieves an even higher *ZT* value of 1.06 under specific doping conditions. These results highlight the potential of the two phases of BaSnS₃ for applications in thermoelectric and optoelectronic technologies.

1 Introduction

As the population grows and industrialization accelerates, the increasing demand for energy highlights the need to explore environmentally sustainable alternative energy sources. Thermoelectric (TE) materials and solar cells are two promising alternative energy technologies, among which thermoelectric materials can directly convert waste heat into electrical energy.[1] By developing thermoelectric materials and devices with high energy conversion efficiency, waste heat from automobile exhausts and industrial processes can be recovered,[2] flexible wearable thermoelectric devices can be manufactured,[3] and new types of thermoelectric generators can be developed.[4] The efficiency of thermoelectric materials is typically expressed by the dimensionless figure of merit (*ZT* value), given by the formula:

$$ZT = \frac{S^2 \sigma T}{k} \quad (1)$$

The Seebeck coefficient is denoted as *S*, electrical conductivity as σ, temperature as *T*, and thermal conductivity as *k*,

which includes both lattice thermal conductivity (k_L) and electronic thermal conductivity (k_e). The *ZT* value of an ideal material should be greater than 1.[5] To achieve a high *ZT* value, a material must possess a high Seebeck coefficient, high electrical conductivity, and low thermal conductivity. However, as these parameters are interdependent, optimizing them simultaneously presents a significant challenge. Methods to enhance the performance of thermoelectric materials mainly focus on balancing the power factor (PF = $S^2 \sigma$) and thermal conductivity. Currently, common approaches include heavy doping, nanostructure, and band structure engineering, which can significantly improve thermoelectric performance.[6,7]

In recent years, perovskite materials have gained widespread attention in thermoelectric research due to their ease of preparation and excellent stability. The general formula of perovskite materials is ABX₃, where the A-site and B-site are occupied by large and small cations, respectively, while the X-site is occupied by anions. Chalcogenide perovskites, in particular, have attracted significant attention in the field of thermoelectric materials due to their high Seebeck coefficient and ultra-low lattice thermal conductivity.[8–10] Numerous experimental and theoretical studies have demonstrated the potential of chalcogenide perovskites in the field of energy conversion.[11,12]

The basic configuration of such materials is ABX₃ [A = Ca, Sr, Ba, Mg; B = Ti, Zr, Sn, Hf; X = S, Se]. Orthorhombic chalcogenide perovskites such as CaZrS₃, BaTiS₃, BaZrS₃, SrTiS₃, and

School of Materials Science and Physics, China University of Mining and Technology, Xuzhou 221116, China. E-mail: 3391@cumt.edu.cn

SrZrS$_3$ have been successfully synthesized.[13,14] In 2022, Song et al.[15] studied CaZrS$_3$ and achieved a maximum ZT value of 4.06 (n-type) and 2.62 (p-type), and in 2023,[16] they found the optimal ZT values of 0.37 (n-type) and 1.52 (p-type) for BaSnO$_3$. In 2024, Yang et al.[17] conducted experimental research on BaZrS$_3$ and found that it had an electron mobility of up to 385 cm^2 V^{-1} s^{-1} at 300 K and a lattice thermal conductivity of 1.11 W m^{-1} K^{-1} at 623 K.

Given that BaSnS$_3$ belongs to the same main group as the materials mentioned above, we predict that it also exhibits excellent thermoelectric properties. Moreover, as research on this material has been limited, we employed self-consistent phonon calculations based on first principles to investigate the effects of anharmonicity on the lattice dynamics and thermal transport of crystalline BaSnS$_3$ at finite temperatures. The calculation process considered double transport channels, isotope phonon scattering, three-phonon (3ph) scattering, and higher-order phonon renormalization. Finally, we obtained a reasonable lattice thermal conductivity (k_L), which, combined with the calculated electronic transport properties, resulted in the final thermoelectric figure of merit. Through this work, we hope to promote further research and application of BaSnS$_3$ and related materials in the field of thermoelectricity.

2 Computational details

The calculations in this study were performed using density functional theory (DFT) implemented in the Vienna Ab initio Simulation Package (VASP) code.[18] The exchange-correlation potential in the form of Perdew–Burke–Ernzerhof (PBE) generalized-gradient approximation (GGA) was applied,[19] and the wave functions were represented using the projector augmented wave (PAW) pseudopotential method.[20] In the structure optimization, a cutoff energy of 500 eV was selected for the plane-wave basis set. Gamma-centered k-point grids of 6 × 13 × 3 and 9 × 7 × 9 were used for α-BaSnS$_3$ and β-BaSnS$_3$, respectively. The convergence criteria for energy and force were set to 1×10^{-8} eV and 1×10^{-6} eV Å^{-1}, respectively. In addition, the Heyd–Scuseria–Ernzerhof (HSE06)[21] hybrid functional was employed to obtain reliable bandgap and optical properties.

The electronic transport properties were calculated using the transport method implemented in the AMSET package, which uses the momentum relaxation-time approximation to calculate the scatter ability and mobility within the Born approximation.[22] The calculation considered acoustic deformation potential (ADP) scattering, ionized impurity (IMP) scattering, and polar optical phonon (POP) scattering. The net relaxation rates are added by Matthiessen's rule:

$$\frac{1}{\tau} = \frac{1}{\tau^{ADP}} + \frac{1}{\tau^{IMP}} + \frac{1}{\tau^{POP}} \quad (2)$$

where τ^{ADP}, τ^{IMP}, and τ^{POP} are the relaxation times of ADP, IMP, and POP scattering, respectively. The differential scattering rate is calculated using Fermi's golden rule:

$$\tau_{n\mathbf{k}\to m\mathbf{k}+\mathbf{q}}^{-1} = \frac{2\pi}{\hbar}|g_{nm}(\mathbf{k},\mathbf{q})|^2\delta(\varepsilon_{n\mathbf{k}} - \varepsilon_{m\mathbf{k}+\mathbf{q}}) \quad (3)$$

where $n\mathbf{k}$ is an initial wavevector and $m\mathbf{k} + \mathbf{q}$ final wavevector after scattering. $\hbar$ is the reduced Planck constant. ε and g are the carrier energy and coupling matrix element, respectively. δ is the Dirac delta function which ensures energy is conserved during the scattering process. The potential matrix element of ADP, IMP, and POP scattering processes is given by:

$$g_{nm}^{ADP}(\mathbf{k},\mathbf{q}) = \left[\frac{k_B T \alpha_v^2}{B_0}\right]^{1/2}\langle\psi_{m\mathbf{k}+\mathbf{q}}|\psi_{n\mathbf{k}}\rangle \quad (4)$$

$$g_{nm}^{IMP}(\mathbf{k},\mathbf{q}) = \left[\frac{n_{ii} Z^2 e^2}{\varepsilon_0}\right]^{1/2}\frac{\langle\psi_{m\mathbf{k}+\mathbf{q}}|\psi_{n\mathbf{k}}\rangle}{|\mathbf{q}|^2 + \beta^2} \quad (5)$$

$$g_{nm}^{POP}(\mathbf{k},\mathbf{q}) = \left[\frac{\hbar\omega_{po}}{2}\left(\frac{1}{\varepsilon_\infty} - \frac{1}{\varepsilon_0}\right)\right]^{1/2}\frac{\langle\psi_{m\mathbf{k}+\mathbf{q}}|\psi_{n\mathbf{k}}\rangle}{|\mathbf{q}|} \quad (6)$$

k_B, α_v, B_0, n_{ii}, Z, ε_∞, ε_0 and ω_{po} are Boltzmann constant, deformation potential, bulk modulus, the concentration of ionized impurities, the charge state of the impurity center, high frequency dielectric constant, static dielectric constant and polar optical phonon frequency respectively. Finally, the electrical transport data were obtained using the 37 × 79 × 21 and 35 × 25 × 37 k-point meshes.

For the phonon thermal transport properties, the interatomic force constants (IFCs) were calculated by the ALAMODE[23,24] package, which uses the relaxation time approximation to solve the Boltzmann transport equation, and the lattice thermal conductivity can be expressed by the following formula:

$$\kappa_p^{\mu\nu} = \frac{1}{VN_\mathbf{q}}\sum_{\mathbf{q}j}C_v(\mathbf{q}j)v^\mu(\mathbf{q}j)v^\nu(\mathbf{q}j)\tau_{\mathbf{q}j} \quad (7)$$

where superscripts μ and ν denote the spatial components (such as x, y, or z), V is the unit cell volume, $N_\mathbf{q}$ is the number of wave vectors, $\mathbf{q}$ is the phonon wavevector, j is the phonon branch index, C_v is the specific heat capacity, v is group velocity, and τ is the phonon lifetime, and κ_c describing tunneling and wavelike of coherent phonons, governed by the Wigner transport equation, is defined as,

$$\kappa_c^{\mu\nu}(T) = \frac{1}{VN_q}\sum_{\substack{q,jj'\\j\neq j'}}\frac{c_{qj}\omega_{qj'} + c_{qj'}\omega_{qj}}{\omega_{qj} + \omega_{qj'}}$$

$$\times v_{\mathbf{q}jj'}^\mu v_{\mathbf{q}jj'}^\nu \frac{\Gamma_{qj} + \Gamma_{qj'}}{\left(\omega_{qj} - \omega_{qj'}\right)^2 + \left(\Gamma_{\mathbf{q}j} + \Gamma_{qj'}\right)^2} \quad (8)$$

For α-BaSnS and β-BaSnS$_3$, second-order interatomic force constants (IFCs) and higher-order force constants were calculated using 2 × 2 × 1 and 2 × 2 × 2 supercells, respectively. The second-order IFCs were obtained via the finite displacement method, while the higher-order IFCs were generated using compressed sensing lattice dynamics (CSLD).[25] Concretely, we use the ab initio molecular dynamics (AIMD) simulations at 300 K to generate multiple snapshots and specify the random displacement length as 0.1 Å on all atoms inside the snapshot structures to capture the random displacement configurations.

Subsequently, these quasi-random structures were then used to fit the required higher-order IFCs.

3 Results and discussion

3.1 Structural and electronic properties

The α and β-BaSnS$_3$ crystallize in an orthorhombic structure with the space group *Pnma* (62) as shown in Fig. 1, the unit cell contains 4 Ba atoms, 4 Sn atoms, and 12 S atoms, exhibiting anisotropy along the *a*, *b*, and *c* axis. α-BaSnS$_3$ consists of corner-sharing [SnS$_6$]$^{2-}$ octahedra interconnected along the *a*, *b*, and *c* axis, with the interstitial spaces filled by Ba^{2+} ions. In contrast, β-BaSnS$_3$ features a distorted orthorhombic perovskite structure. The structural stability of perovskite materials is typically determined by the Goldschmidt[26] tolerance factor *t*:

$$t = \frac{r_A + r_X}{\sqrt{2}(r_B + r_X)} \qquad (9)$$

In the formula, r_A, r_B, and r_X represent the ionic radii of the A, B, and X ions, corresponding to the radii of Ba^{2+}, Sn^{4+}, and S^{2-}, respectively. An ideal cubic perovskite has a Goldschmidt tolerance factor $t = 1$. The value of *t* can be used to some extent to evaluate the stability of the perovskite crystal structure. Most perovskites form within the range of $0.71 < t < 1.10$. Due to the ionic size matching among the constituent elements, perovskite compounds can adopt different crystal structures. Generally, when $0.90 < t < 1.00$, the perovskite structure tends to have better stability. As shown in Table 1, the *t* of BaSnS$_3$ is 0.911. In addition, the phonon dispersions of the two materials at 0 K were calculated (see ESI, Fig. S1†), and the absence of imaginary frequencies confirms their dynamical stability.

Table 1 also presents the optimized lattice constants and mechanical properties of the two compounds. Notably, the lattice constants of α-BaSnS$_3$ are in close agreement with the experimental values.[27] Using the Voigt–Reuss–Hill (VRH)[28] averaging approximation, the bulk modulus *B*, Young's modulus *Y*, Poisson's ratio ν, and the shear modulus *G* were calculated. The bulk modulus *B*, shear modulus *G*, and Young's

Table 1 The lattice constants (*a*, *b*, and *c*), tolerance factor (*t*), bulk modulus (*B*), shear modulus (*G*), Young's modulus (*Y*), Poisson's ratio (ν), and Debye temperature (θ_D) for α and β-BaSnS$_3$

Parameters	α-BaSnS$_3$	β-BaSnS$_3$
a^{opt}/a^{exp} (Å)	8.61/8.53	7.22
b^{opt}/b^{exp} (Å)	3.99/3.93	10.18
c^{opt}/c^{exp} (Å)	14.80/14.52	7.09
t	0.911	0.911
B (GPa)	49.53	56.16
G (GPa)	27.03	24.22
B/G	1.83	2.32
Y (GPa)	68.61	63.52
ν	0.27	0.31
θ_D (K)	270	261

modulus *Y* provide information on the material's compressibility, resistance to deformation, and stiffness. Significant differences in mechanical properties are observed between the two structures. The bulk modulus of β-phase (56.16 GPa) is higher than that of the α-phase (49.53 GPa), indicating stronger resistance to compression. In comparison, the α-phase demonstrates higher stiffness and shear resistance, with a shear modulus of 27.03 GPa *versus* 24.22 GPa and a Young's modulus of 68.61 GPa compared to 63.52 GPa. This makes it better suited for applications demanding mechanical stability. Conversely, the β-BaSnS$_3$ offers greater ductility and flexibility, as reflected in its higher B/G of 2.32 compared to 1.83, and a Poisson's ratio of 0.31 *versus* 0.27, making it an excellent choice for developing flexible thermoelectric modules.

We conducted a study on the Debye temperatures of these two materials. The Debye temperatures of the α and β-BaSnS$_3$ are 270 K and 261 K, respectively, both of which are relatively low, suggesting that these phases may exhibit lower lattice thermal conductivity. This is due to the presence of heavier elements in the material, which decreases the phonon vibration frequency, thereby lowering the Debye temperature. Additionally, lower phonon frequencies generally also result in lower
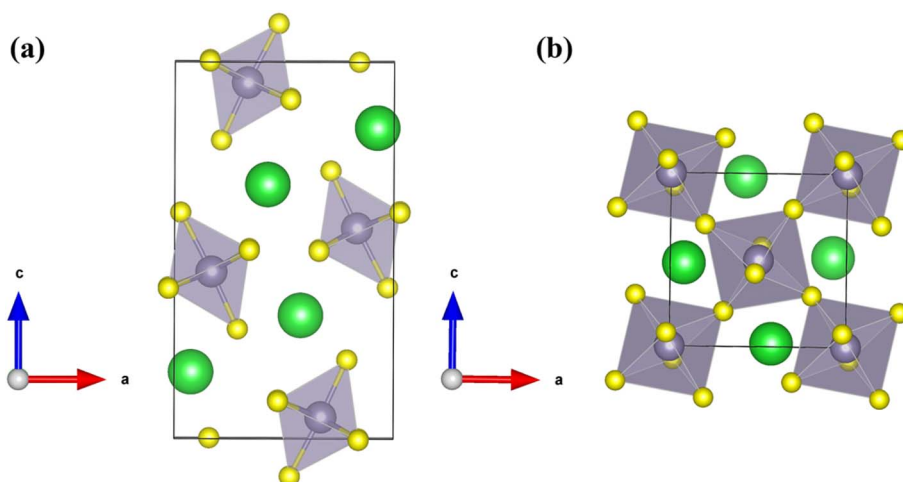
Fig. 1 The crystal structures of (a) α-BaSnS$_3$ and (b) β-BaSnS$_3$, with yellow for S, gray for Sn, and green for Ba.
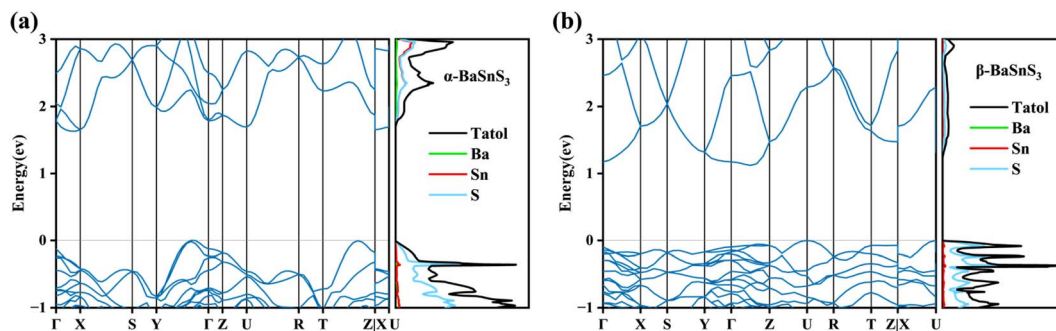
Fig. 2 Band structures and densities of states of (a) α-BaSnS₃ and (b) β-BaSnS₃.

Table 2 Effective masses of holes and electrons for α and β-BaSnS₃

		m_x	m_y	m_z
α-BaSnS₃	e	1.168	0.262	0.678
	h	0.425	0.653	1.192
β-BaSnS₃	e	0.329	0.605	0.836
	h	0.979	1.282	1.549

thermal conductivity.[29] This value is lower than that of some common chalcogenide compounds, such as $CaZrSe_3$, which has a Debye temperature of 450 K and an average lattice thermal conductivity of 1.17 W mK^{-1} at 300 K, with a maximum ZT value of 1.004.[30] However, the actual lattice thermal conductivity is also influenced by other factors, such as phonon scattering.

Fig. 2 presents the band structure and density of states (DOS) calculated using the HSE06 functional for the two structures, with the band gaps of the α and β phases of BaSnS₃ being 1.63 eV and 1.12 eV, respectively. Both are indirect band gap semiconductors and both the conduction band and valence band exhibit band degeneracy. However, the valence band shows a more complex multi-valley structure. This high degree of degeneracy indicates a higher Seebeck coefficient,[31] suggesting that p-type doping could result in a larger Seebeck coefficient.

In addition, the projected density of states (PDOS) was calculated to analyze the contributions of different atomic orbitals. For both structures, the conduction band shows comparable contributions from S and Sn atoms, while the valence band is predominantly contributed by S atoms, indicating that the heavy holes are mainly located around the S atoms. The calculated effective masses of carriers are shown in Table 2. For both structures, the effective mass of holes is overall larger than that of electrons, which may result in lower mobility and require heavy doping to improve performance.

3.2 Optical properties

The optical properties of a material can be analyzed to assess its potential applications in the field of optoelectronics. Fig. 3 examines the optical properties of α-BaSnS₃ and β-BaSnS₃, focusing on dielectric function $\varepsilon(\omega)$, absorption coefficient $\alpha(\omega)$, refractive index $n(\omega)$, energy loss factor $L(\omega)$, and reflectivity $R(\omega)$. The dielectric function $\varepsilon(\omega)$ is divided into two parts $\varepsilon(\omega) = \varepsilon_1(\omega) + i\varepsilon_2(\omega)$, where $\varepsilon_1(\omega)$ denotes the real part and $\varepsilon_2(\omega)$ denotes the imaginary part of the dielectric function, respectively. The aforementioned parameters can be represented using the equations[12] provided below:

$$\varepsilon_1(\omega) = 1 + \frac{2}{\pi} p \int_0^\infty \frac{\omega' \varepsilon_2(\omega')}{\omega'^2 - \omega^2} d\omega' \qquad (10)$$

$$\varepsilon_2(\omega) = \frac{Ve^2}{2\pi\hbar m^2\omega^2} \int d^3k \sum_{nn'} |\langle kn|\hat{p}|kn'\rangle|^2 f(kn)\left[1 - f\left(kn'\right)\right]\hat{\delta}\left(E_{kn} - E_{kn'} - \hbar\omega\right) \qquad (11)$$

$$\alpha(\omega) = \frac{\omega}{c}\sqrt{2\left(\sqrt{\varepsilon_1^2(\omega) + \varepsilon_2^2(\omega)} - \varepsilon_1(\omega)\right)} \qquad (12)$$

$$R(\omega) = \left|\frac{\sqrt{\varepsilon_1(\omega) + i\varepsilon_2(\omega)} - 1}{\sqrt{\varepsilon_1(\omega) + i\varepsilon_2(\omega)} + 1}\right|^2 \qquad (13)$$

$$n(\omega) = \sqrt{\frac{\sqrt{\varepsilon_1^2(\omega) + \varepsilon_2^2(\omega)} + \varepsilon_1(\omega)}{2}} \qquad (14)$$

$$L(\omega) = \frac{\varepsilon_2(\omega)}{\left[\varepsilon_1(\omega)^2 + \varepsilon_2(\omega)^2\right]} \qquad (15)$$

In eqn (10), p is the principal value of the integral, ω is the frequency. In eqn (11), $\hbar\omega$ denotes the energy of the incident photon, while p represents the momentum operator. The eigenfunction corresponding to the eigenvalue E_{kn} is denoted by $|kn\rangle$ and $f(kn)$ signifies the Fermi distribution function.
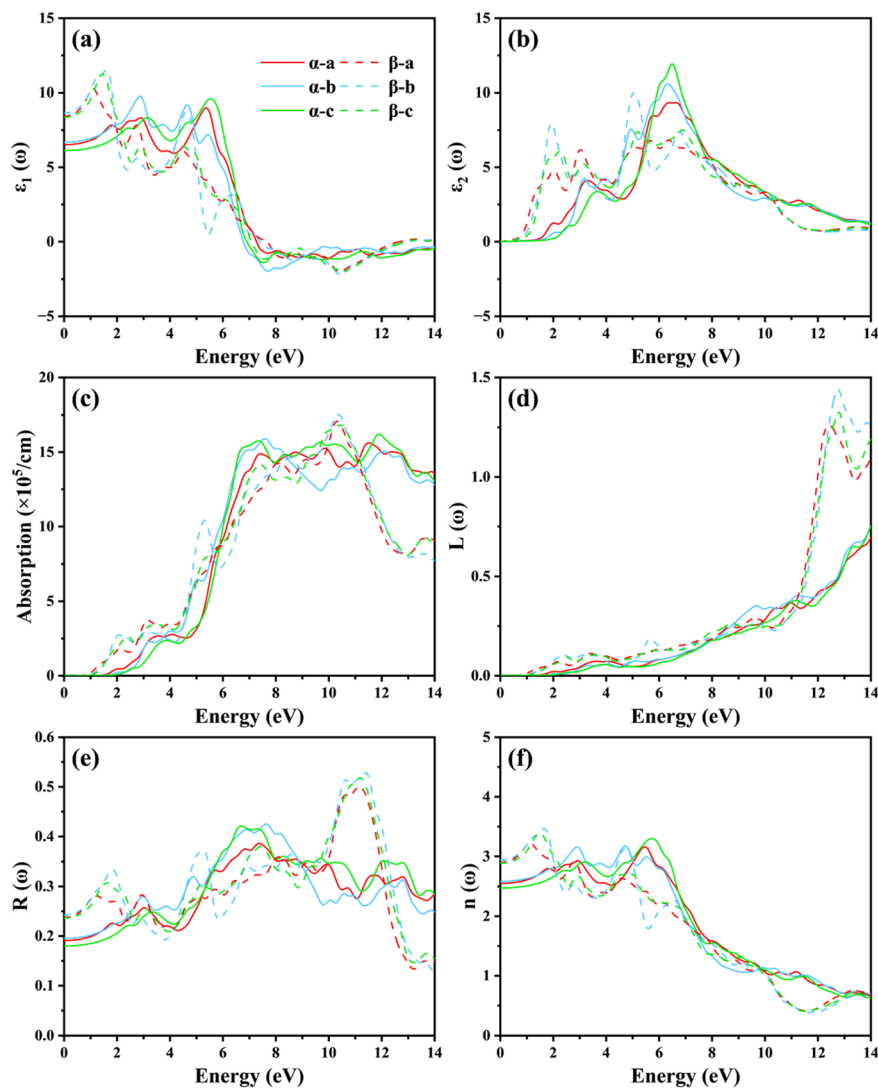
Fig. 3 Optical properties of α-BaSnS$_3$ and β-BaSnS$_3$, including (a) real part of the dielectric function, (b) imaginary part of the dielectric function, (c) optical absorption coefficient, (d) energy loss function, (e) reflectivity, and (f) refractive index.

The dielectric function is a key physical parameter that characterizes how a material responds to electromagnetic waves. Fig. 3(a) and (b) depict the real and imaginary components of the dielectric function. The real part, ε_1, represents the material's ability to store energy from an electric field. At zero frequency, the real part of the dielectric function, $\varepsilon_1(\omega)$, is referred to as the static dielectric constant. The static dielectric constants of α-BaSnS$_3$ and β-BaSnS$_3$ are 6.44 and 8.47, respectively. The real part of the dielectric functions of α-BaSnS$_3$ and β-BaSnS$_3$ exhibits multiple peaks within the energy range of 0–6 eV, which result from effective electronic transitions from the valence band to the conduction band. For α-BaSnS$_3$, the coordinates of the highest two peaks of the real part of the dielectric function are (2.89, 8.32) and (5.37, 8.99) in a-axis; (2.87, 9.78) and (4.64, 9.18) in the b-axis; (3.17, 8.32) and (5.57, 9.61) in the c-axis. For β-BaSnS$_3$, they are (1.07, 10.27) and (2.73, 7.83); (1.61, 11.52) and (4.66, 8.71); (1.48, 11.22) and (4.54, 6.41). As the

photon energy increases, the values gradually decrease and eventually become negative.

The imaginary part, ε_2, measures the material's ability to absorb energy from the electric field and is directly linked to the bandgap. For α-BaSnS$_3$ and β-BaSnS$_3$, it can be seen that there is no significant absorption within their bandgap range (1.63 eV and 1.12 eV). Their $\varepsilon_2(\omega)$ peak energies are approximately 6.49 eV and 5.05 eV. The absorption coefficient of a material measures its ability to capture light, which directly impacts the power conversion efficiency of solar cells. High absorption coefficients are crucial for such applications. As shown in Fig. 3(c), when the energy of the photon equals the bandgap of the material, absorption of the incident photon will occur. The two materials have similar absorption coefficients in the energy range of 0–10 eV. For the α structure, the absorption coefficient in all directions increases with photon energy, exhibiting an absorption peak around 7.5 eV, with a value of approximately 1.5×10^6 cm^{-1}. Afterward, small fluctuations occur as the
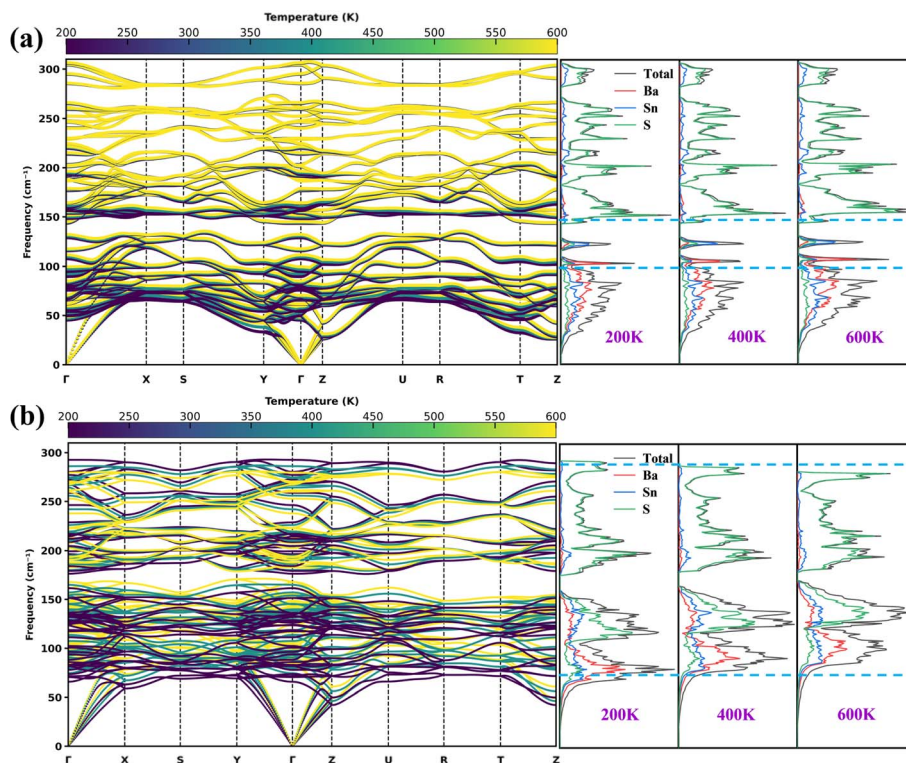
Fig. 4 Phonon dispersion and density of states for (a) α-BaSnS$_3$ and (b) β-BaSnS$_3$ at 200 K, 400 K, and 600 K.

energy continues to rise. In the case of the β structure, the *a*, *b*, and *c* directions each show two prominent absorption peaks within the 0–14 eV range. The first peak corresponds to photon energies and absorption coefficients of 8.1 eV $(1.43 \times 10^6 \text{ cm}^{-1})$, 5.3 eV $(1.04 \times 10^6 \text{ cm}^{-1})$, and 7.3 eV $(1.41 \times 10^6 \text{ cm}^{-1})$, respectively. Their second peak is observed around 10.4 eV, with a magnitude of approximately $1.75 \times 10^6 \text{ cm}^{-1}$.

Fig. 3(d) presents the energy loss as a function of photon energy. For both materials, the energy loss is minimal in the low photon energy region but increases to a maximum in the high photon energy region, corresponding to where $\varepsilon_1(\omega)$ approaches zero. Beyond 12 eV, the energy loss function of β-BaSnS$_3$ becomes significantly larger than that of α-BaSnS, likely due to its lower reflectivity within this energy range. The reflectivity and refractive index are two important parameters necessary for solar applications. The reflectivity gives a measure of reflecting light or

radiation. In contrast, the refractive index reflects the material's transparency. As shown in Fig. 3(e) and (f), the average static reflectivity values for α-BaSnS$_3$ and β-BaSnS$_3$ are 19% and 24%, respectively, with maximum values in the *b* direction of 43% and 53%. For the refractive index, it exhibits a trend similar to that of the real part of the dielectric function, with multiple peaks appearing within the 0–6 eV range. The average static refractive index values for α-BaSnS$_3$ and β are 2.54 and 2.91, respectively, with maximum values of 3.30 (in the *c*-axis) corresponding to an energy of 5.78 eV, and 3.47 (in the *b*-axis) corresponding to an energy of 1.73 eV. Overall, their high absorption coefficients make them widely applicable in photocatalytic water splitting for hydrogen production, environmental purification, and optoelectronic devices such as photodetectors and phototransistors. The high refractive index also makes them suitable for thin-film-based optoelectronic devices.
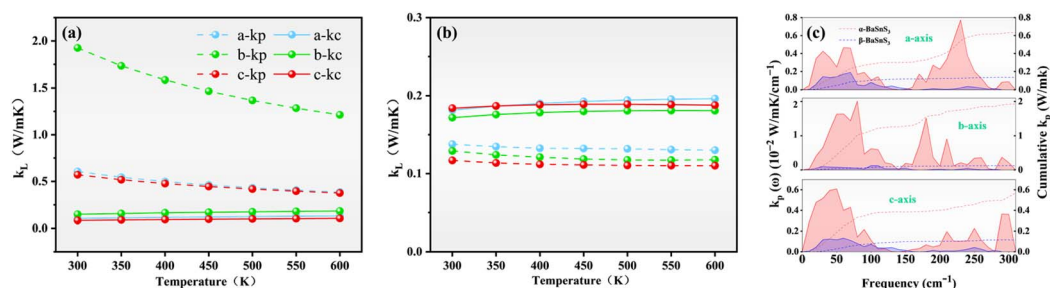

Fig. 5 Lattice thermal conductivity of (a) α-BaSnS$_3$ and (b) β-BaSnS$_3$ as a function of temperature; (c) thermal conductivity spectra and cumulative thermal conductivity along the *a*, *b*, and *c*-directions at 300 K.

3.3 Phonon dispersion and lattice thermal conductivity

We examined the impact of temperature on the phonon dispersion of the structures. As illustrated in Fig. 4(a) and (b), an upward shift of the phonon modes in the low-frequency region is observed for both structures as the temperature increases, a phenomenon known as phonon hardening. Similar hardening of optical phonon modes has also been reported in analogous perovskite structures.[32–34] In the high-frequency region (200 cm^{-1}–310 cm^{-1}), the phonon dispersion of the α-BaSnS$_3$ remains largely unaffected by temperature. In contrast, the phonon hardening observed in the β-BaSnS$_3$ gradually diminishes with increasing frequency and ultimately
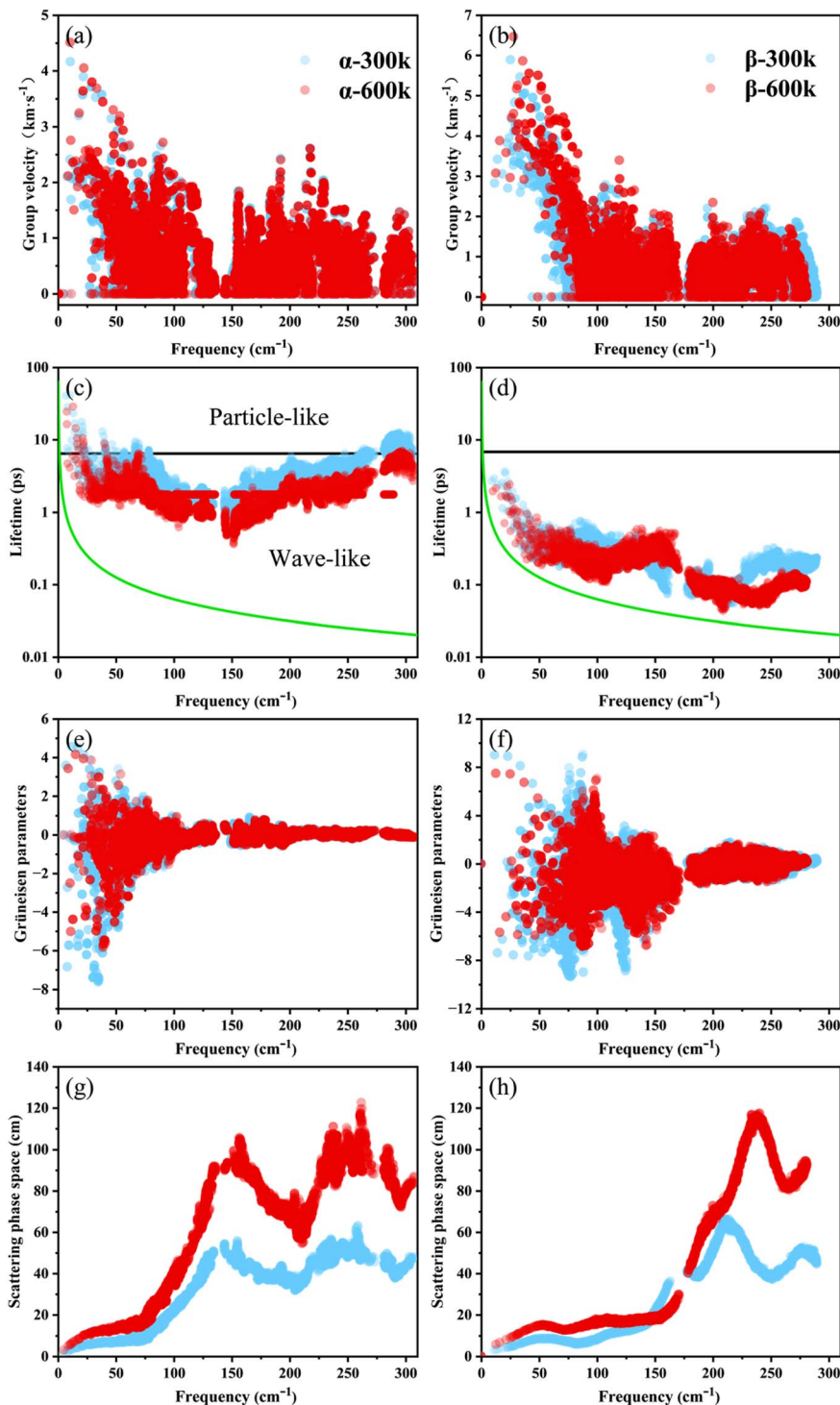

Fig. 6 Calculated Phonon group velocity (a and b), phonon lifetime (c and d) (the black solid line illustrates the Wigner limit, while the green curve indicates the Ioffe–Regel limit), Grüneisen parameter (e and f), and three-phonon scattering phase space (g and h) as a function of frequency at 300 K and 600 K.

transitions into a softening phenomenon. Fig. 4 also shows the corresponding density of states at different temperatures, and the shifts in the peak positions also reflect a similar hardening trend in the mid-to low-frequency phonon dispersion. In the high-frequency region, the phonons are mainly contributed by the vibrations of S atoms, while the low-frequency optical and acoustic regions are dominated by Ba and Sn atoms.

Fig. 5(a) and (b) illustrates the temperature dependence of k_L for the α and β-BaSnS$_3$. We calculated the lattice thermal conductivity using the particle-like propagation and wave-like tunneling transport channels, respectively. At 300 K, the k_p of the α-phase along the a, b, and c directions is 0.61, 1.93, and 0.57 W m^{-1} K^{-1}, respectively, with an average value of 1.03 W m^{-1} K^{-1}. The average value of the k_c is 0.112 W m^{-1} K^{-1}. For the β-phase, the corresponding values are 0.138(k_p-a), 0.129(k_p-b), 0.117(k_p-c), 0.128(k_p-average), 0.179(k_c-average) W m^{-1} K^{-1}. To quantify the importance of the low-frequency modes, the cumulative thermal conductivity relative to frequency is calculated. Fig. 5(c) present the thermal conductivity spectra and cumulative thermal conductivity for the two structures along the a, b, and c directions at 300 K, respectively. For the α-BaSnS$_3$, both high-frequency and low-frequency phonon modes play a substantial role in determining the lattice thermal conductivity. In comparison, the lattice thermal conductivity of the β-BaSnS$_3$ is mainly contributed by phonons in the low-to-mid frequency range (0–150 cm^{-1}).

On the other hand, it can be observed that the thermal conductivity of both structures is quite low. Moreover, for the β structure, the proportion of the k_c in the total thermal conductivity is substantial. We then study some phonon properties to investigate the underlying causes. As shown in eqn (7), group velocity and phonon lifetime(τ) directly influence the lattice thermal conductivity. Fig. 6 further examines the phonon properties relevant to this relationship at 300 K and 600 K. Fig. 6(a) and (b) illustrate the group velocities of the two structures. For both structures, the group velocities are predominantly concentrated below 2 km s^{-1}. The low V_{ph} can be ascribed to the flat phonons in most q spaces.[35] In addition, the group velocities in the high-frequency region are generally lower than those in the low-frequency region. The heavier Ba atoms in the material lead to a lower group velocity. Within the frequency range corresponding to phonon dispersion hardening, the group velocity increases slightly with rising temperature, which is attributed to anharmonic phonon renormalization leading to an upshift of the low-frequency phonon modes. Nevertheless, the extremely low lattice thermal conductivity of the β-BaSnS$_3$ remains unexplained. To further investigate, we proceeded to calculate the phonon lifetimes of the structure. As shown in Fig. 6(c) and (d), the phonon lifetimes of the α-BaSnS$_3$ are predominantly in the range of 1–10 ps, whereas those of the β-BaSnS$_3$ are an order of magnitude lower, concentrated in the range of 0.1–1 ps. We propose that these extremely short
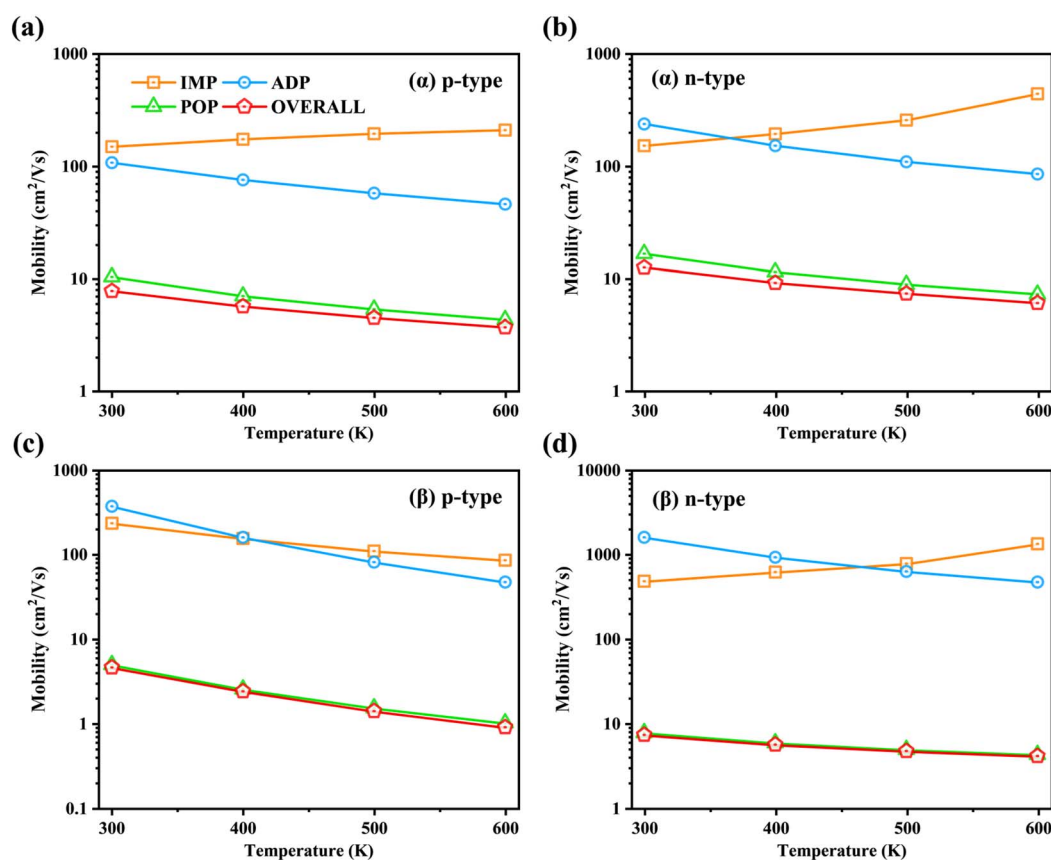

Fig. 7 The overall and scattering mechanism resolved mobilities for n-type and p-type doping as a function of temperature. All the results have a doping concentration of 1×10^{19} cm^{-3}. (a and b) α-BaSnS$_3$; (c and d) β-BaSnS$_3$.

phonon lifetimes are the primary reason for the ultralow lattice thermal conductivity of β-BaSnS₃.

A recent breakthrough introduces the concept of the Wigner time limit to classify phonons into different thermal transport behaviors: particle-like propagation and wavelike tunneling.[36] As shown by the black solid line in the Fig. 6(c) and (d). The limit is defined as $\tau_{\text{Wigner}} = 3N_{\text{at}}/\omega_{\text{max}}$, where N_{at} is the number of atoms in the unit cell and ω_{max} is the maximum phonon frequency. The green curve shows the Ioffe-Regel limit, $\tau_{\text{Ioffe-Regel}} = 2\pi/\omega$, in which ω is the phonon frequency. Phonon lifetime exceeding $\tau_{\text{Ioffe-Regel}}$ can be described by the Wigner transport equation. Phonons with $\tau > \tau_{\text{Wigner}}$ behave as particle-like phonons that contribute mainly to κ_p, whereas the large phonons population with $\tau_{\text{Ioffe-Regel}} < \tau < \tau_{\text{Wigner}}$ displays wave-like phonons feature that contributes mainly to κ_c. For the α-BaSnS₃, most phonons have lifetimes below the Wigner limit at 300 K, whereas for the β-BaSnS₃, all phonon lifetimes fall below this limit, underscoring the significance of wavelike tunneling as a transport channel. Moreover, this also explains why, in the β-BaSnS₃, k_c exceeds k_p. To obtain a deeper understanding of the microscopic mechanisms of the wavelike phonon tunneling thermal transport, we plot three-dimensional visualizations of

the mode-specific contribution to κ_c at 300 K. As shown in Fig. S2,† the quasi-degenerate eigenstates ($\omega 1 \approx \omega 2$) contribute most to κ_c because the smaller the energy difference between eigenstates, the stronger the wavelike tunneling effect that is produced.[37]

To investigate the origin of the extremely low phonon lifetimes in the β-BaSnS₃, we calculated the Grüneisen parameter (γ) for both compounds, with the results shown in Fig. 6(e) and (f). According to the Debye model, the phonon lifetime (τ) is inversely proportional to the square of γ. In the low-to-mid frequency range, both compounds exhibit relatively large absolute values of γ, with a maximum value near 8 for the α-BaSnS₃ and 10 for the β-BaSnS₃, indicating strong anharmonicity in both materials. Beyond 150 cm⁻¹, γ converges toward zero, suggesting that high-frequency optical phonon modes contribute minimally to anharmonicity. Additionally, the large negative values of γ indicate that both compounds are likely to undergo negative thermal expansion upon heating.[38] For a more detailed investigation, γ is further mapped onto the phonon dispersion along high-symmetry paths (refer to Fig. S3 in the ESI†). For the α-BaSnS₃, it is evident that only the acoustic and low-frequency optical phonon modes exhibit relatively large γ
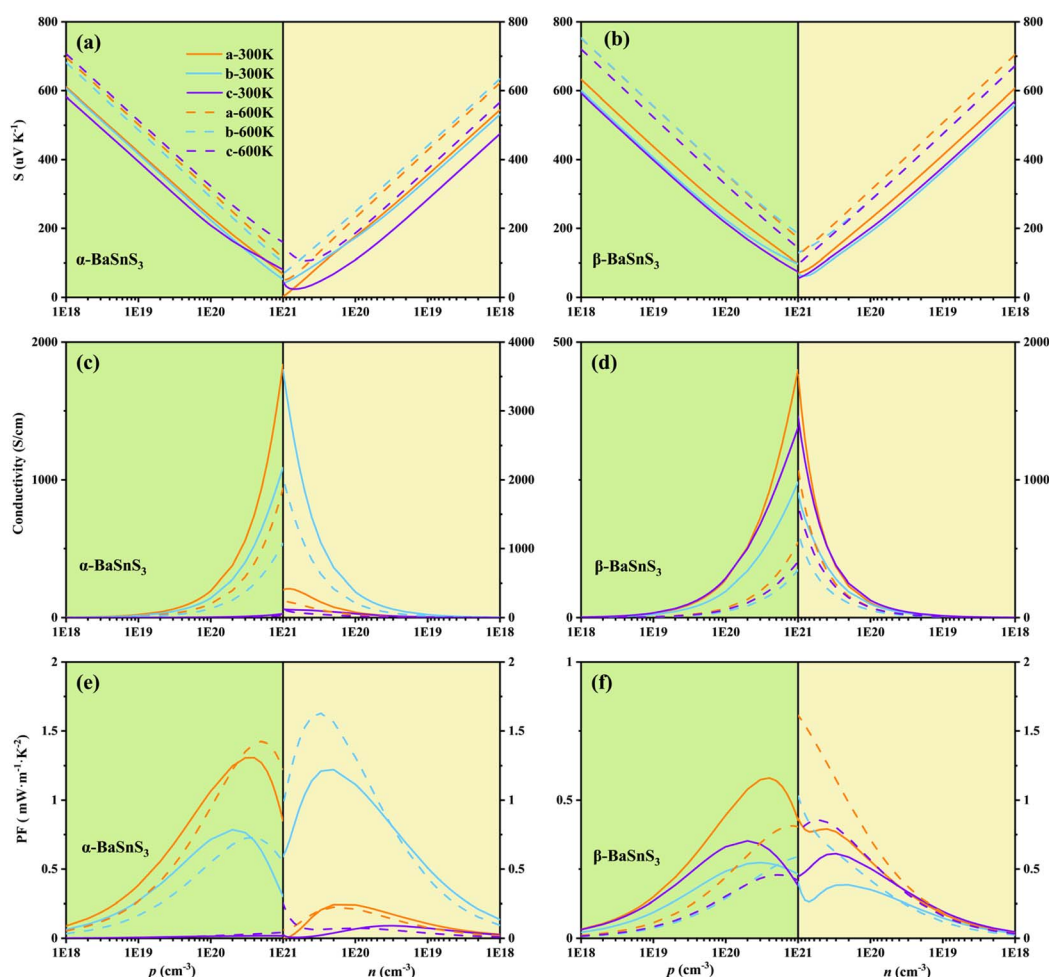

Fig. 8 Electrical transport properties at 300 K and 600 K: (a and b) the absolute value of the Seebeck coefficient, (c and d) electrical conductivity, and (e and f) power factor.

values, while the γ values for phonon modes in other frequency ranges are nearly zero. In contrast, for the β-BaSnS₃, phonon modes below 150 cm⁻¹ generally show large γ values, with the maximum values observed in the acoustic modes. This indicates strong anharmonicity, which significantly enhances three-phonon scattering processes. Moreover, the corresponding Grüneisen parameter decreases significantly with increasing temperature.

Finally, the three-phonon scattering phase space of the materials was calculated, as shown in Fig. 6(g) and (h). The three-phonon scattering phase space (SPS) increases significantly as the temperature rises from 300 K to 600 K. This is due to the increase in phonon occupancy and the enhancement of anharmonicity with rising temperature, leading to more three-phonon scattering processes and simultaneously reducing phonon lifetime. By considering anharmonic phonon renormalization, the SPS shifts to higher frequency regions (phonon hardening), while its amplitude decreases, which is consistent with the decrease phonon lifetimes observed in the calculations in Fig. 6(c) and (d). In summary, the low group velocity and short phonon lifetimes, primarily caused by the high anharmonicity in the low-frequency region, are the key contributors to the low lattice thermal conductivity of both materials. This effect is particularly pronounced in the β-BaSnS₃.

3.4 Electronic properties and figure of merit

In this study, we considered ADP, POP, and IMP scattering mechanisms to investigate the electronic transport properties of p-type and n-type carriers. The relevant input parameters can be found in the ESI.† We further examined the temperature dependence of carrier mobility at a fixed doping concentration of 1×10^{19} cm⁻³, as illustrated in Fig. 7. For both structures, the contributions of ADP and IMP are 1 to 2 orders of magnitude larger than that of POP, and the smaller POP contribution results in a reduction in the total mobility. Comparing the total mobility of α-BaSnS₃ at room temperature, which is 7.8 cm² V⁻¹ s⁻¹ for p-type carriers and 12.6 cm² V⁻¹ s⁻¹ for n-type carriers, it is evident that β-BaSnS₃ is more significantly impacted, with its total mobility at room temperature being suppressed to 4.6 cm² V⁻¹ s⁻¹ for p-type carriers and 7.3 cm² V⁻¹ s⁻¹ for n-type carriers. The electrons' mobility is relatively higher than that of the holes, substantiating that for n-doping.

Fig. 8 illustrate the Seebeck coefficient, electrical conductivity, and power factor as functions of carrier concentration for both p-type and n-type doping at temperatures of 300 K and 600 K, which is highly similar to the results obtained by Li *et al.*[39] Specifically, Fig. 8(a) and (b) show that the absolute value of the Seebeck increases, while it rises with increasing temperature. This trend is consistent with the theoretical formula:[40]
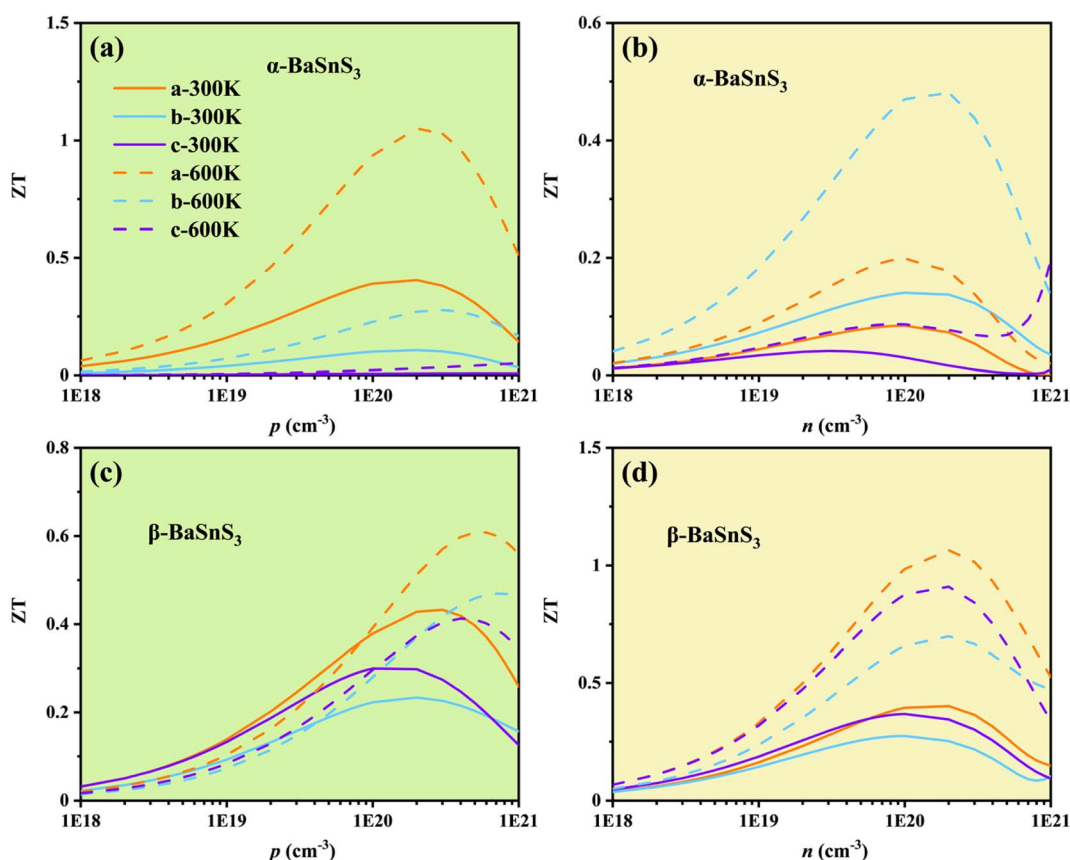

Fig. 9 Thermoelectric figure of merit (ZT) as a function of carrier concentration at 300 K and 600 K for n-type and p-type doping, respectively. (a and b) α-BaSnS₃; (c and d) β-BaSnS₃.

$$S = \frac{\Delta V}{\Delta T} = \frac{2K_B^2 m^* T}{3e\hbar^2} \left(\frac{\pi}{3n}\right)^{2/3} \qquad (16)$$

where V, e, m^*, and n represent the voltage, electron charge, effective mass, and charge carrier concentration, respectively. The maximum Seebeck coefficients of $BaSnS_3$ at 300 K are 611 $\mu V\ K^{-1}$ for p-type and 545 $\mu V\ K^{-1}$ for n-type in the α-phase, and 633 $\mu V\ K^{-1}$ for p-type and 607 $\mu V\ K^{-1}$ for n-type in the β-phase, respectively.

Fig. 8(c) and (d) present the electrical conductivity of the α and β-$BaSnS_3$. Electrical conductivity (σ) is directly dependent on carrier mobility (μ), as described by the equation, $\sigma = ne\mu$. Similar to mobility, σ decreases as temperature increases. However, an increase in carrier concentration also results in a rise in σ. From Fig. 7, it can be seen that the mobility of the α-$BaSnS_3$ is higher than that of the β-$BaSnS_3$. Therefore, the electrical conductivity of the α-$BaSnS_3$ is also greater, with its maximum value being approximately twice that of the β-$BaSnS_3$.

Moreover, the PF as a function of carrier concentration at different temperatures, is instrumental in determining the optimal doping level for maximizing thermoelectric performance. PF increases with carrier concentration, reaching a peak value and then decreasing as illustrated in Fig. 8(e) and (f). The maximum power factors (PF) of the α-$BaSnS_3$ are 1.43 mW m^{-1} K^{-2} for p-type and 1.63 mW m^{-1} K^{-2} for n-type, while those of the β-phase are 0.58 mW m^{-1} K^{-2} for p-type and 1.61 mW m^{-1} K^{-2} for n-type.

We calculated the ZT values of $BaSnS_3$ along different crystallographic directions, varying with carrier concentration and temperature, as depicted in Fig. 9. Both structures reach their maximum ZT values at 600 K. Under specific carrier concentrations, the maximum ZT observed in α-$BaSnS_3$ for p-type is 1.05, which is higher than that of its n-type. Similarly, For ZT of the β-$BaSnS_3$ is found to be 0.61 for p-type and 1.06 for n-type. These maximum ZT are attained along the a-axis.

4　Conclusions

This study systematically explores the mechanical, optical, and thermoelectric properties of α-$BaSnS_3$ and β-$BaSnS_3$ using first-principles calculations. The β-phase demonstrates superior ductility and flexibility, as evidenced by its higher B/G ratio (2.32) and Poisson's ratio (0.31), making it a promising candidate for flexible device applications. Both phases exhibit moderate bandgaps of 1.63 eV (α-phase) and 1.12 eV (β-phase), as well as high absorption coefficients ($\sim 1 \times 10^6$ cm^{-1}) in the ultraviolet region, highlighting their potential for optoelectronic applications.

In terms of thermal transport, the α-phase shows an average lattice thermal conductivity of 1.03(k_p) and 0.112(k_c) W m^{-1} K^{-1} at 300 K, while the β-phase achieves an exceptionally low value of 0.128(k_p) and 0.197(k_c)W m^{-1} K^{-1}, making it advantageous for thermoelectric applications. The electrical transport properties were studied at 300 K and 600 K. For α-$BaSnS_3$, the p-type ZT surpasses the n-type, reaching a maximum of 1.05 along the a-axis. In contrast, the β phase exhibits relatively higher ZT values for n-type carriers, reaching 1.06 along the a-axis. In summary, these findings provide a theoretical foundation for their use in waste heat recovery, solar energy harvesting, and flexible electronic devices.

Data availability

The data supporting this article have been included as part of the ESI.† The data that support the findings of this study are available from the corresponding author upon reasonable request.

Conflicts of interest

There are no conflicts to declare.

Acknowledgements

References

1 S. Zhan, L. Zheng, Y. Xiao and L.-D. Zhao, *Chem. Mater.*, 2020, **32**, 10348–10356.
2 S. Mandal and P. Sarkar, *J. Mater. Chem. C*, 2023, **11**, 13691–13706.
3 Q. Yang, S. Yang, P. Qiu, L. Peng, T.-R. Wei, Z. Zhang, X. Shi and L. Chen, *Science*, 2022, **377**, 854–858.
4 R. Wang, M. Wu, D. Jiang, H. Liang, W. He, Y. Sun and Z. Qian, *Adv. Electrode Mater.*, 2023, **9**, 2300300.
5 E. Osei-Agyemang, C. E. Adu and G. Balasubramanian, *npj Comput. Mater.*, 2019, **5**, 116.
6 M. Li, N. Wang, M. Jiang, H. Xiao, H. Zhang, Z. Liu, X. Zu and L. Qiao, *J. Mater. Chem. C*, 2019, **7**, 11029–11039.
7 N. Wang, M. Li, H. Xiao, Z. Gao, Z. Liu, X. Zu, S. Li and L. Qiao, *npj Comput. Mater.*, 2021, **7**, 18.
8 H. Shahmohamadi and S. S. Naghavi, *ACS Appl. Mater. Interfaces*, 2021, **13**, 14189–14197.
9 S. Niu, J. Milam-Guerrero, Y. Zhou, K. Ye, B. Zhao, B. C. Melot and J. Ravichandran, *J. Mater. Res.*, 2018, **33**, 4135–4143.
10 Z. Huo, S.-H. Wei and W.-J. Yin, *J. Phys. D: Appl. Phys.*, 2018, **51**, 474003.
11 K. V. Sopiha, C. Comparotto, J. A. Márquez and J. J. S. Scragg, *Adv. Opt. Mater.*, 2022, **10**, 2101704.
12 M. Ju, J. Dai, L. Ma and X. C. Zeng, *Adv. Energy Mater.*, 2017, **7**, 1700216.
13 A. Clearfield, *Acta Crystallogr.*, 1963, **16**, 135–142.
14 S. Perera, H. Hui, C. Zhao, H. Xue, F. Sun, C. Deng, N. Gross, C. Milleville, X. Xu, D. F. Watson, B. Weinstein, Y.-Y. Sun, S. Zhang and H. Zeng, *Nano Energy*, 2016, **22**, 129–135.
15 X. Song, X. Shai, S. Deng, J. Wang, J. Li, X. Ma, X. Li, T. Wei, W. Ren, L. Gao, Y. Fu, H. Wang and C. Zeng, *J. Phys. Chem. C*, 2022, **126**, 11751–11760.
16 X. Song, G. Wang, L. Zhou, H. Yang, X. Li, H. Yang, Y. Shen, G. Xu, Y. Luo and N. Wang, *ACS Appl. Energy Mater.*, 2023, **6**, 9756–9763.

17 Z. Yang, Y. Han, Y. Liang, W. Shen, Z. Zhang, C. Fang, Q. Wang, B. Wan, L. Chen, Y. Zhang and X. Jia, *Acta Mater.*, 2024, **276**, 120156.

18 G. Kresse and J. Furthmüller, *Phys. Rev. B:Condens. Matter Mater. Phys.*, 1996, **54**, 11169–11186.

19 J. P. Perdew, K. Burke and M. Ernzerhof, *Phys. Rev. Lett.*, 1996, **77**, 3865–3868.

20 P. E. Blöchl, *Phys. Rev. B:Condens. Matter Mater. Phys.*, 1994, **50**, 17953–17979.

21 J. Heyd, J. E. Peralta, G. E. Scuseria and R. L. Martin, *J. Chem. Phys.*, 2005, **123**, 174101.

22 A. M. Ganose, J. Park, A. Faghaninia, R. Woods-Robinson, K. A. Persson and A. Jain, *Nat. Commun.*, 2021, **12**, 2222.

23 T. Tadano and S. Tsuneyuki, *Phys. Rev. B:Condens. Matter Mater. Phys.*, 2015, **92**, 054301.

24 T. Tadano, Y. Gohda and S. Tsuneyuki, *J. Phys.: Condens. Matter*, 2014, **26**, 225402.

25 F. Zhou, B. Sadigh, D. Åberg, Y. Xia and V. Ozoliņš, *Phys. Rev. B*, 2019, **100**, 184309.

26 V. M. Goldschmidt, *Naturwissenschaften*, 1926, **14**, 477–485.

27 S. Yamaoka and B. Okai, *Mater. Res. Bull.*, 1970, **5**, 789–794.

28 W. Voigt, *Lehrbuch der Kristallphysik*, Vieweg+Teubner Verlag, Wiesbaden, 1966.

29 Y. Yu, M. Cagnoni, O. Cojocaru-Mirédin and M. Wuttig, *Adv. Funct. Mater.*, 2020, **30**, 1904862.

30 E. Osei-Agyemang, C. E. Adu and G. Balasubramanian, *npj Comput. Mater.*, 2019, **5**, 116.

31 J. Zhang, L. Song, S. H. Pedersen, H. Yin, L. T. Hung and B. B. Iversen, *Nat. Commun.*, 2017, **8**, 13901.

32 V. Železný, E. Cockayne, J. Petzelt, M. F. Limonov, D. E. Usvyat, V. V. Lemanov and A. A. Volkov, *Phys. Rev. B:Condens. Matter Mater. Phys.*, 2002, **66**, 224303.

33 S. Glinšek, D. Nuzhnyy, J. Petzelt, B. Malič, S. Kamba, V. Bovtun, M. Kempa, V. Skoromets, P. Kužel, I. Gregora and M. Kosec, *J. Appl. Phys.*, 2012, **111**, 104101.

34 M. A. Helal, T. Mori and S. Kojima, *Appl. Phys. Lett.*, 2015, **106**, 182904.

35 F. Xiao, Q.-Y. Xie, X. Ming, H. Li, J. Zhang and B.-T. Wang, *Phys. Rev. B*, 2024, **109**, 245202.

36 M. Simoncelli, N. Marzari and F. Mauri, *Nat. Phys.*, 2019, **15**, 809–813.

37 Y. Xia, V. I. Hegde, K. Pal, X. Hua, D. Gaines, S. Patel, J. He, M. Aykol and C. Wolverton, *Phys. Rev. X*, 2020, **10**, 041029.

38 M. T. Dove, Z. Wei, A. E. Phillips, D. A. Keen and K. Refson, *APL Mater.*, 2023, **11**, 041130.

39 Z. Li, H. Xie, Y. Xia, S. Hao, K. Pal, M. G. Kanatzidis, C. Wolverton and X. Tang, *Chem. Mater.*, 2022, **34**, 1289–1301.

40 G. Tan, L.-D. Zhao and M. G. Kanatzidis, *Chem. Rev.*, 2016, **116**, 12123–12149.